Heat diffusion across magnetic islands and ergodized plasma regions in realistic tokamak geometry

M. Hölzl, S. Günter, and the ASDEX Upgrade Team

Max-Planck-Institut für Plasmaphysik, EURATOM Association, 85748 Garching, Germany

ABSTRACT

Heat diffusion in magnetized plasmas is investigated numerically for tokamak geometry and realistic plasma parameters. Heat transport across single and overlapping magnetic islands is studied. As an application, the influence of an (n+1,m+1) helical perturbation onto the temperature perturbation caused by an (n,m) neoclassical tearing mode (NTM) is examined. It is shown that the resulting ergodization of the magnetic field structure is able to reduce the resonant bootstrap current perturbation of a neoclassical tearing mode. This might explain the drop in the mode amplitude observed in the frequently interrupted regime (FIR-NTMs). Furthermore, the influence of edge ergodization as generated by external perturbation coils onto the electron temperature is studied. It is shown that ergodization of the plasma boundary can decrease the pedestal temperature gradient significantly. This effect might be one element in the mitigation effects of edge localized modes (ELMs) achieved by external resonant perturbation fields.

I. INTRODUCTION

Heat diffusion processes play a crucial role for instabilities like neoclassical tearing modes (NTMs) [1] and are connected to mitigation of edge localized modes (ELMs) by resonant magnetic field perturbations [2]. We examine heat diffusion processes across magnetic islands and ergodic layers in realistic tokamak geometry and highlight the possible role of stochastisation for neoclassical tearing modes in the frequently interrupted regime (FIR-NTMs) [3]. At the plasma boundary, we investigate the effect of ergodization by external perturbation coils on the temperature profile.

The physical, mathematical, and numerical model used in this article is explained in Sec. II. Sec. III deals with heat diffusion across single magnetic islands. Effective radial heat transport is compared to cylindrical results, and the temperature structures at the island x-point are compared to electron cyclotron emission spectroscopy measurements (ECE). Subsequently, in Sec. IV, heat transport across ergodic layers and the possible role of stochastisation for FIR-NTMs is discussed. Heat diffusion across an ergodized plasma boundary is investigated in Sec. V.

II. MODEL

A. Heat Diffusion Tensor

As charged particles have a much higher mobility parallel to magnetic field lines than perpendicular to them, the magnetic topology influences heat transport tremendously. This can be described by an anisotropic heat diffusion tensor. Its component perpendicular to the magnetic field lines, $\chi_\perp$, usually is dominated by anomalous transport and of the order $1\mathrm{m}^2/\mathrm{s}$, whereas its component parallel to the magnetic field lines, $\chi_{||}$, is much larger and can be described by Spitzer-H¨arm diffusivity,

$$\chi_{||}^{SH} = 3.16 \cdot v_{th,e} \cdot \lambda_e, \tag{1}$$

where $v_{th,e} = \sqrt{T_e/m_e}$ is the electron thermal velocity, λ_e the collisional electron mean free path, T_e the electron temperature, and m_e the electron mass [4, 5]. Temperatures are measured in units of energy in this article assuming the Boltzmann constant k_B as an implicit prefactor. Eq. (1) is valid in the collisional regime only, where λ_e is much smaller than the scale length L of temperature gradients. This is usually only the case in a thin layer around the separatrix of magnetic islands.

If $\lambda_e \gtrsim L$, heat transport is dominated by convection, and the temperature becomes non-local. It has been shown, that heat transport can still be described as a diffusive process using the “heat flux limit”, i.e. limiting the heat flux to a fraction of the value for free-streaming electrons [6] by using

$$\chi_{||}^{limit} = L \cdot v_{th,e} \tag{2}$$

everywhere, where the heat flux according to Spitzer-H¨arm diffusivity would exceed this limit otherwise. Chang and Callen derived $L \approx 1/|k_{||}|$ with a theoretical approach, where $k_{||}$ denotes the parallel wave number [7, 8]. This length scale is comparable to the distance along a field line between the poloidal positions of the island x- and o-points. We apply the heat flux limit correction using the analytical matching

$$\chi_{||}^{hfl} = \left(\chi_{||}^{SH}\chi_{||}^{limit}\right) / \left(\chi_{||}^{SH} + \chi_{||}^{limit}\right) \tag{3}$$

between the limits of Eqs. (1) and (2) as done similarly before [8, 9].

B. Heat Diffusion Equation

The steady-state anisotropic heat diffusion equation,

$$\nabla \cdot \vec{q} = P, \tag{4}$$

$$\vec{q} = -n_e \left[\chi_{||}\nabla_{||}T + \chi_{\perp}\nabla_{\perp}T\right] = -n_e\chi_{\perp} \left[\chi\nabla_{||}T + \nabla T\right], \tag{5}$$

is solved numerically, where $\vec{q}$ denotes the heat flux (density), n_e the electron density, P the energy source term, $\hat{b} = \vec{B}/B$ the magnetic field direction vector, $\nabla_{||}T = \hat{b}(\hat{b}\cdot\nabla T)$ the parallel temperature gradient, $\chi_{\perp}$ resp. $\chi_{||}$ the heat diffusion coefficient perpendicular resp. parallel to

Table 1: Assumptions made in this article for physical parameters.

Topic	**Equilib.**	$\mathbf{n_e}$	$\chi_\perp$	$\chi_{\|\|}$	$\mathbf{B_{pert}}$	**boundary cond.**
Island heat transport	#15863	const	const	const	analyt.	$T(0.8)$
Comparison of X-point with experiment	#11681	const	$\chi_\perp(\rho)$	$\chi_{\|\|}^{hfl}$	analyt.	$\frac{\partial T}{\partial \rho}\|_{\rho=0.3}, T(0.8)$
Ergodic Layer, FIR-NTMs	#15863	const	const	const	analyt.	$T(0.8)$
Ergodic Edge	#15863	$n_e(\rho)$	$\chi_\perp(\rho)$	$\chi_{\|\|}^{SH}$	coils	$\frac{\partial T}{\partial \rho}\|_{0.8}, T(1.1)$

the magnetic field lines, and $\chi = (\chi_{||} - \chi_\perp)/\chi_\perp$ the heat diffusion anisotropy. In tensor notation, Eqs. (4) and (5) may be written as

$$\frac{1}{\sqrt{g}} \frac{\partial}{\partial u^\alpha} (\sqrt{g} q^\alpha) = P, \tag{6}$$

$$q^\alpha = -n_e \chi_\perp \left[\chi b^\alpha b^\beta + g^{\alpha\beta} \right] \frac{\partial T}{\partial u^\beta}, \tag{7}$$

where $\vec{e}_\alpha$ resp. $\vec{e}^\alpha$ denote the co- and contravariant basis-vectors, $g_{\alpha\beta}$ resp. $g^{\alpha\beta}$ components of the metric tensors, $g = \det[g_{\alpha\beta}]$, and $b^\alpha = \vec{e}^\alpha \cdot \hat{b}$ are contravariant components of the magnetic field direction vector. As this formulation does not presume flux or straight field line coordinates, arbitrary coordinate systems can be used in principle. The coordinate systems actually employed in our investigations are described in Sec. E.

C. Physical Assumptions

Table 1 briefly lists assumptions made for the relevant physical parameters of this article. The following paragraphs explain these in some more detail. All computations are performed for the geometry of the ASDEX Upgrade tokamak [10]. We use axisymmetric ideal magneto-hydrodynamic (MHD) equilibria reconstructed from experiment using the VMEC/NEMEC code [11, 12].

Magnetic perturbation fields used for island heat transport examinations (Sec. III) and for investigations related to heat transport across ergodic layers (Sec. IV) are determined assuming simple radial perturbation profiles. The perturbation field used in Sec. V for the ergodic plasma boundary is determined from Ampères law using the geometry of the coil set [13] projected to be installed at ASDEX Upgrade. We neglect the plasma response to magnetic perturbations (vacuum approximation). As discussed in Ref. [14], external perturbation fields are shielded by plasma rotation, which we account for by reducing the coil currents by a factor of about five from the values aimed at in the experiment. This way, an ergodic boundary of about 10% of the minor radius is produced as seen from Fig. 8.

We assume heating is localized to the plasma core to avoid local heat sources inside magnetic islands for simplicity. As the electron density gradient is usually small in the plasma core and large at the edge, a realistic profile must only be used for plasma boundary computations. Constant electron density is assumed for all core plasma cases.

The perpendicular heat diffusivity is assumed to be constant except for the direct comparison of the island x-point structures to experimental data and for the ergodized plasma boundary. For these cases, $\chi_\perp$ was adapted to reproduce the unperturbed experimental temperature profiles.

We assume constant $\chi_{||}$ for most computations, as Spitzer-Härm diffusivity is virtually constant in most cases due to temperature flattening. As this is not the case for the plasma boundary, we use a radial profile for the Spitzer-Härm diffusivity according to Eq. (1) there. For comparing the island x-point structures to the experiment, we perform computations for both the Spitzer-Härm diffusivity and the heat flux limit according to Eq. (3).

If the radial interval $\rho = \rho_{min} \ldots \rho_{max}$ covered by a code run starts at $\rho_{min} = 0$, Eqs. (4) and (5) can be integrated over a small volume around the magnetic axis to obtain a boundary condition. Otherwise Neumann boundary conditions are used at ρ_{min}. At ρ_{max}, Dirichlet boundary conditions are applied for all cases.

D. Numerical Scheme

We solve Eqs. (4) and (5) with a finite difference approach developed in Ref. [15, 16]. This scheme requires two staggered grids, which we call T- resp. q-grids as the temperature is defined on one grid and the heat flux on the other. The q-grid is shifted against the T-grid by half a grid point distance in all three dimensions. In contrast to other schemes, this method allows to perform heat diffusion computations with realistic values of χ (which may reach values of 10^{10} in the core plasma) in coordinate systems with no coordinate line parallel to the magnetic field lines. This is especially important, if permanently adapting the coordinate system in time-dependent computations becomes too expensive or if exactly aligned global coordinate systems do not exist as for ergodic cases or calculations extending across the plasma separatrix.

E. Coordinate System

Rough coordinate alignment is still desireable with the scheme described in Sec. D, as it allows to reduce the required resolution in one coordinate direction. To achieve this, an axisymmetric straight field line coordinate system is employed which is determined by the equilibrium code package used. It can be described by

$$R(\rho,\theta,\phi) = \sum_m \left[R_m(\rho)\sin[\zeta_m(\theta,\phi)] + \tilde{R}_m(\rho)\cos[\zeta_m(\theta,\phi)] \right], \tag{8}$$

$$\Phi = \phi, \tag{9}$$

$$Z(\rho,\theta,\phi) = \sum_m \left[Z_m(\rho)\sin[\zeta_m(\theta,\phi)] + \tilde{Z}_m(\rho)\cos[\zeta_m(\theta,\phi)] \right], \tag{10}$$

where (ρ,θ,ϕ) denote the curvlinear coordinate system used, (R,Φ,Z) cylindrical coordinates, and $\zeta_m(\theta,\phi) = m\theta$. The radial coordinate ρ may be transformed for grid refinement. Coordinate alignment can be achieved by replacing $\zeta_m(\theta,\phi)$ with $m(\theta - \iota_c\phi)$, thus, transforming the straight field line coordinate system to a helical one. In principle, ι_c can be an arbitrary function of the radial coordinate ρ. But only for constant

$$\iota_c = k/G_\theta, \tag{11}$$

where G_θ denotes the poloidal grid point number and k an arbitrary integer number, grid points at $\phi = 2\pi$ do coincide with grid points at $\phi = 0$. In all other cases, an interpolation is required to implement the toroidal periodicity condition $T(\phi+2\pi) = T(\phi)$. As we found the numerical errors caused by this interpolation to be inacceptably large for realistic values of χ, only ι_c according to Eq. (11) are used. This allows to align the basis vector $\vec{e}_\phi$ to the unperturbed magnetic field lines of the flux surface at which the safety factor q is equal to $1/\iota_c$.

For all other flux surfaces, the coordinate system is misaligned by $\Delta\iota(\rho) = |\iota_c - \iota(\rho)|$, where $\iota(\rho) = q(\rho)^{-1}$ denotes the inverse safety factor. To investigate numerical errors, computations for a large $m/n = 3/2$ magnetic island ($w = 6.3\mathrm{cm}$ and $w/w_c = 7.7$; see Sec. III and Ref. [1] for a definition of these quantities) have been performed with different values of ι_c and different poloidal and toroidal grid point numbers. Here, m and n denote the poloidal and toroidal mode numbers. Fig. 1 shows the numerical error in the dominant Fourier component of the temperature, $T_{3/2}$, normalized to the unperturbed temperature vs. the misalignment $\Delta\iota$ for a fixed number of $129 \times 129 \times 23$ radial, poloidal and toroidal grid points. First, a moderate increase of numerical errors is observed as $\Delta\iota$ increases, but at $\Delta\iota \approx G_\phi/G_\theta$, where G_θ resp. G_ϕ denote the poloidal and toroidal grid point numbers, the error drops again. Here, the magnetic field direction is aligned to the diagonal of the grid cells. For even larger $\Delta\iota$, errors increase strongly, which implies a restriction $\Delta\iota \lesssim G_\phi/G_\theta$ to resolve magnetic islands well. Thus, for $3/2$ and $4/3$ islands $G_\phi \gtrsim 0.05 G_\theta$ is the minimum requirement when chosing $\iota_c = 5/7$, while in a purely toroidal coordinate system ($\iota_c = 0$), $G_\phi \gtrsim 0.75 G_\theta$ would be much more expensive.

To be able to compare core plasma effects like island heat diffusion to cylindrical results, we introduce the minor radius $r(\rho) = \sqrt{A(\rho)/\pi}$, where $A(\rho)$ is the surface area confined by

$\rho = \mathrm{const}$ in a $\phi = \mathrm{const}$ plane. This allows to determine the so-called critical island width w_c analogously to the cylinder using the analytical formulae derived by Fitzpatrick [1]. The island width w can be determined as the difference between the values of $r(\rho)$ at the outer- and innermost positions of the island separatrix.

The straight field line coordinate system used for the core plasma is not well-suited for edge computations. At the low field-side close to the separatrix, it has a low poloidal resolution and the radial and poloidal basis vectors $\vec{e_\rho}$ and $\vec{e_\theta}$ are almost parallel. Furthermore, the option of a helical coordinate system for approximate alignment is not vital in this domain as the field lines are predominantly oriented in toroidal direction. For these reasons, we use a different coordinate system for edge computations, where θ is taken to be the real poloidal angle and the $\rho = \mathrm{const}$ surfaces at $\rho \leq \rho_{cut}$ are flux surfaces. The surfaces corresponding to $\rho > \rho_{cut}$ are continued linearly which allows to use a single coordinate system for both, the plasma and the vacuum regions. The surface corresponding to the chosen ρ_{cut} is located about $1\mathrm{cm}$ inside the separatrix at the low-field side.

III. ISLAND HEAT TRANSPORT

The formation of magnetic islands by reconnection of field lines is a resistive process [17], which may be triggered by instabilities (tearing modes) or resonant external perturbation fields. Temperature gradients within island flux surfaces are reduced to a degree depending on the ratio between the island width w and the critical island width $w_c \propto \chi^{-1/4}$ [1]. For typical values of w and χ, the temperature inside the separatrix of an island flattens in the absence of local heat sources. This can be observed from the experiment using electron cyclotron emission spectroscopy (ECE) [18]. Fig. 2 shows numerical results for temperature and heat flux density at a large $3/2$ island (width about 13 percent of the minor radius) for different values of χ resp. w/w_c. For $w/w_c \gtrsim 2$, the temperature flattens completely at the island o-point. With increasing w/w_c, the flattened region gradually extends towards the island separatrix and the heat flux, accordingly, becomes localized to a thin heat conduction layer around the island separatrix.

For a periodic cylinder, the relative increase of the effective radial heat diffusivity,

$$\chi_\rho^+ = \frac{\chi_\rho}{\chi_{\rho,unpert}} - 1 = \frac{\partial T_{unpert}/\partial \rho}{\partial T/\partial \rho} - 1, \tag{12}$$

at the resonant surface of a magnetic island depends on w/w_c only and features two different regimes [1, 19, 20]. Fig. 3 shows the dependence of χ_ρ^+ on w/w_c for two different island cases in realistic tokamak geometry and compares them to results for periodic cylindrical geometry.

The almost perfect agreement between the two different islands in tokamak geometry proves that island heat transport depends on w/w_c only as shown by Fitzpatrick for cylindrical geometry [1]. However, comparing to cylindrical results reveals differences up to 25% and slightly different dependencies on w/w_c. This might be caused by differing “local” values of w/w_c at the low and high field sides in toroidal geometry. Fig. 3 also contains analytical predictions by Yu derived for small islands in cylindrical geometry [19].

ECE measurements allow to investigate the temperature of magnetic islands with mode frequencies below the Nyquist frequency [18]. The standard sample frequency of the ECE diagnostic at ASDEX Upgrade is not high enough for $3/2$ NTMs yet, but will soon be improved. However, a limited number of discharges is already available, though radial resolution and calibration do not suffice for quantitative comparisons of radial profiles to numerical simulations. But timetraces of single ECE channels resolve poloidal “cuts” through the islands. After averaging these over about 100 periods to reduce noise, we study the structures observed close to the resonant surface. As seen from Fig. 2, the width of these structures along θ direction (and also their height) depends on the anisotropy of the heat diffusion tensor.

With the available radial resolution, a characteristic distribution of the measured structures can be expected. This is due to the variable distance of the closest ECE channel from the resonant surface. Fig. 4 shows height ΔT vs. width $\Delta\theta$ of these structures at randomly chosen timepoints, where timepoints located around FIR-crashes, with exceptionally large noise or with differing heating powers were excluded. The distributions represented by the dashed, solid and dotted curves correspond to numerical simulations using parallel heat diffusivities $\chi_{||}^{SH}$, $\chi_{||}^{hfl}$ resp. $\chi_{||}^{hfl}/4$ (see Sec. II). The following observations can be made from Fig. 4:

- Good agreement with heat flux limit computations is observed for both investigated discharges with different island sizes. The fraction of datapoints which directly agrees with the numerical results within the estimated error bars is 60% resp. 50% for the two discharges. All other data points are located to the “right” of resp. “below” the predicted distribution. This is plausible, as the averaging process can increase $\Delta\theta$ and decrease ΔT in response to small errors in mode phase determination.
- The fraction of data points which directly agrees with computations using Spitzer-Härm diffusivity is lower at 30% resp. 45% and all data points which do not agree are also

shifted to the “right”.

- If the data points are compared to numerical results obtained using $\chi_{||}^{hfl}/4$ as the parallel heat diffusivity, an agreement of only 30% is observed for both discharges. Disagreeing data points are mostly located “left” of the numerically determined distribution. Whereas less pronounced structures can easily be obtained by slight phase shift errors, larger temperature gradients along θ should not occur accidently.

We can therefore conclude that the experimental measurements are fully compatible with numerical results produced using $\chi_{||}^{hfl}$ as parallel heat diffusivity. Agreement with results for $\chi_{||}^{SH}$ is worse but cannot be ruled out completely, while parallel diffusivities significantly lower than $\chi_{||}^{hfl}$ cannot explain the experimental data.

IV. ERGODIC LAYERS AND FIR-NTMS

Flattening of the temperature profile inside magnetic islands causes large bootstrap current perturbations, which amplify the initial magnetic perturbation thus destabilizing the magnetic island which is called an NTM then [1, 20]. At high values of the normalized plasma pressure β_N, a frequent interruption of the NTM growth by a sudden drop of the mode amplitude has been observed such that the mode cannot saturate (FIR-NTM) [3]. This effect has been shown to be linked to three wave-coupling [21] and alleviates the average confinement degradation [22]. While the NTM grows on a long time scale of the order of $50\ \mathrm{ms}$, the amplitude drop takes only about $1\ \mathrm{ms}$, which might be caused by field stochastisation from the interaction with another mode locked to the NTM [21]. For an m/n NTM, this is usually an $m+1/n+1$ mode. Here, m and n denote the poloidal and toroidal mode numbers. Although it is unlikely that the mode responsible for the field ergodization creates an island at its rational surface, for simplicity we discuss the overlapping of two magnetic islands in the following. The degree of field stochastisation caused by $3/2$ and $4/3$ islands is measured by the Chirikov parameter [23, 24]

$$\sigma_{Ch} = (w_{3/2} + w_{4/3})/[2(r_{3/2} - r_{4/3})], \tag{13}$$

where $w_{m/n}$ and $r_{m/n}$ denote the island width corresponding to an m/n island resp. the minor radius of its rational surface. Ergodic heat transport is still dominated by single island effects for small w/w_c, but strongly enhanced vs. these for large w/w_c. In the latter case, the temperature profile over the whole ergodic region flattens [19, 20], as seen from Fig. 5 for different values of χ and fixed island sizes $w_{3/2} = 8.1\mathrm{cm}$ and $w_{4/3} = 5.1\mathrm{cm}$. The corresponding heat flux densities are also plotted.

Temperature flattening in the ergodic region reduces the resonant bootstrap current perturbation of the $3/2$ NTM significantly and therefore also the island drive. We examine this effect for a $3/2$ NTM with $w = 8.1\mathrm{cm}$ and an additional $4/3$ perturbation of variable amplitude which corresponds to a σ_{Ch} scan. Part (a) of Fig. 6 shows the first derivative of the temperature mode $T_{3/2}$ for different values of σ_{Ch} at $\chi = 10^9$. It can be seen, that $dT_{3/2}/d\rho$ is strongly reduced for $\sigma_{Ch} \gtrsim 1.2$. In part (b) of this figure, the dependence of the averaged absolute value of $dT_{3/2}/d\rho$ in the island region,

$$|dT_{3/2}/d\rho|_{av} = \frac{\int_{0.4}^{0.54} d\rho \; |dT_{3/2}/d\rho|}{\int_{0.4}^{0.54} d\rho}, \tag{14}$$

is shown for three different values of χ. This quantity is suppressed strongly by stochastisation for $\sigma_{Ch} \gtrsim 1.2$ and large heat diffusion anisotropies. It can be concluded, that the resonant bootstrap current perturbation $j_{b,3/2} \propto dT_{3/2}/d\rho$ is strongly reduced due to field ergodisation. This can happen on a timescale much faster than the typical resisitive timescale as the stochastisation enables a fast decay of the bootstrap current perturbation along magnetic field lines.

The effect of ergodization by overlapping magnetic islands on the effective radial heat transport is presented in Fig. 7. The relative increase χ_ρ^+ of the radial heat diffusivity (see Eq. (12)) at the $7/5$ rational surface is plotted and compared to the sum of the separate effects of $4/3$ and $3/2$ islands. For large values of χ, a strong increase of radial heat diffusivity is observed which corresponds to the flattening of the whole ergodic region shown in Fig. 5.

V. ERGODIC PLASMA BOUNDARY

Perturbation field coils have been installed at several tokamak devices like DIII-D [25] and TEXTOR [26] which can be used to ergodize the plasma boundary. This has been shown to be capable of ELM mitigation (edge localized modes) [27, 28]. The transport of electrons along stochastic field lines is an important element in this process and leads e.g. to an increased heat conduction [2]. At the example of the active coil set projected for ASDEX Upgrade [13], we investigate the possibility of the effect of an ergodic magnetic field on temperature gradients. The magnetic field generated by the “n=4 plus/minus phasing” of the coil set is used neglecting the plasma response to the perturbation. To account for plasma shielding, the coil currents are reduced in return (see Sec. II for details). In addition to the ergodization of the field close to the edge (about 10 percent of the minor radius), we observe some impact on the plasma shape (see Fig. 8). The plasma “grows” somewhat towards the upper divertor.

The large gradients of the pedestal region and the separatrix geometry make this problem computationally very demanding. The straight field line coordinate system used for plasma core examinations is not well-suited for edge examinations. Computations for realistic plasma parameters are possible only with a special coordinate system which uses the real angle as poloidal coordinate (see Sec. II for details). As we are interested in the pedestal region only, $\chi_\perp$ is chosen unrealistically large in the scrape-off layer to simplify convergence. From Figs. 9 and 10, a clear reduction of pedestal temperature gradients is observed which reduces the pedestal height by about 20 percent.

VI. CONCLUSIONS

Numerical heat diffusion computations are demonstrated in real tokamak geometry for realistic plasma parameters both for the plasma core and the plasma boundary. The numerical scheme used allows to perform these computations with coordinate systems where no basis vector is parallel to the magnetic field direction. At the plasma core, we use unsheared helical straight field line coordinates to reduce the required toroidal resolution. This way, magnetic islands and even ergodic layers can be examined for realistic values of the parallel heat conductivity.

Comparing our results for heat transport across magnetic islands with experimental measurements indicates that the heat diffusivity in fusion plasmas is essentially in agreement with the values predicted by the heat flux limit. More detailed comparisons between theory and experiments are beyond the scope of this paper but will be published elesewhere.

To find an explanation for the amplitude drops in the FIR-NTM regime, the effect of stochastisation on the first temperature harmonic was studied. The resonant bootstrap current perturbation has been shown to be strongly suppressed if the Chirikov parameter $\sigma_{Ch} \gtrsim 1.2$ and the heat diffusion anisotropy is large enough.

For the plasma edge, we use a simple flux coordinate system inside the plasma and extend it continuously into the scrape-off layer. This way, we are able to examine the effect of edge ergodization on heat transport and observe a significant reduction of the temperature gradients in the pedestal region.

VII. ACKNOWLEDGEMENTS

The authors would like to thank Qingquan Yu, Marc Maraschek, Wolfgang Suttrop, Erika Strumberger and Karl Lackner for helpful discussions.

References

[1] R. Fitzpatrick. Phys. Plasmas **2**, 825 (1995).

[2] M. Bécoulet, G. Huysmans, P. Thomas, P. Ghendrih, A. Grosman , P. Monier-Garbet, X. Garbet, W. Zwingman, E. Nardon, and R. Moyer *20th IAEA Fusion Energy Conference, Vilamoura, Portugal, 2004* (International Atomic Energy Agency, Vienna, 2004), TH/1-3Rc.

[3] S. G¨unter, A. Gude, M. Maraschek, S. Sesnic, H. Zohm, ASDEX Upgrade Team, and D. F. Howell. Phys. Rev. Letters **87**, 275001-1 (2001).

[4] L. Spitzer and R. H¨arm. Phys. Rev. **89**, 977 (1953).

[5] S. I. Braginskii. Reviews of Plasma Physics, **1**, 204 (1965).

[6] R. C. Malone, R. L. McCrory, and R. L. Morse. Phys. Rev. Lett. **34**, 721, (1975).

[7] Z. Chang and J. D. Callen. Phys. Fluids B **4**, 1182 (1992).

[8] Q. Yu, S. G¨unter, G. Giruzzi, K. Lackner, M. Zabiego. Phys. Plasmas **7**, 312 (2000).

[9] M. Z. Tokar and A. Gupta. Phys. Rev. Lett. **99**, 225001 (2007).

[10] A. Hermann and O. Gruber. Fusion Sci. Technol **44**, 569 (2003).

[11] S.P. Hirshman, and D.K. Lee. Comput. Phys. Commun. **39** 161 (1986).

[12] S.P. Hirshman, W.I. van Rij, and P. Merkel. Comput. Phys. Commun. **43** 143 (1986).

[13] W. Suttrop, and T. Bertoncelli, and V. Bobkov, and O. Gruber and A. Herrmann and P. Merkel and M. Rott and M. Sempf and U. Seidel and B. Streibl and E. Strumberger

and T. Vierle and D. Yadikin and Q. Yu and B. Unterberg and M. Lehnen and E. Gaio and V. Toigo and P. Brunsell and J. Drake and ASDEX Upgrade Team. Europhysics Conference Abstracts (CD-ROM), Proc. of the 34th EPS Conference on Controlled Fusion and Plasma Physics, Warsaw, Poland, 2007, edited by Pawel Gasior and Jerzy Wolowski (European physical society, Geneva, 2007), Vol 31F, p. P5.119.

[14] Q. Yu, S. Günter, Y. Kikuchi, and K. H. Finken. Nucl. Fusion **48** 024007 (2008).

[15] S. Günter, Q. Yu, J. Krüger, and K. Lackner. J. Comput. Phys. **209**, 354 (2005).

[16] S. Günter, K. Lackner, and C. Tichmann. J. Comput. Phys. **226**, 2306 (2007).

[17] H. P. Furth, J. Killeen, M. N. Rosenbluth. Phys. Fluids **6**, 459 (1963).

[18] J. P. Meskat, H. Zohm, G. Gantenbein, S. Günter, M. Maraschek, W. Suttrop, Q. Yu, and ASDEX Upgrade Team. Plasma Phys. Control. Fusion, **43**, 1325 (2001).

[19] Q. Yu. Phys. Plamas **13**, 062310 (2006).

[20] M. Hölzl, S. Günter, Q. Yu., and K. Lackner. Phys. Plamas **14**, 052501 (2007).

[21] A. Gude, S. Günter, M. Maraschek, H. Zohm, and ASDEX Upgrade Team. Nucl. Fusion **42**, 833 (2002).

[22] S. Günter, M. Maraschek, M. de Baar, D. F. Howell, E. Poli, E. Strumberger, C. Tichmann, ASDEX Upgrade Team, and Contributors to the EFDA-JET Workprogramme. Nucl. Fusion **44**, 524, (2004).

[23] B. V. Chirikov. Phys. Rep. **52** 263 (1979).

[24] Ph. Ghendrih, A. Grosman, and H. Capes. Plasma Phys. Control. Fusion **38**, 1653 (1996).

[25] J. L. Luxon. Nucl. Fusion **42**, 614 (2002).

[26] U. Samm. Fusion Sci. Technol **47**, 73 (2005).

[27] T. E. Evans, R. A. Moyer, P. R. Thomas, J. G. Watkins, T. H. Osborne, J. A. Boedo, E. J. Doyle, M. E. Fenstermacher, K. H. Finken, R. J. Groebner, M. Groth, J. H. Harris, R. J. La Haye, C. J. Lasnier, S. Masuzaki, N. Ohyabu, D. G. Pretty, T. L. Rhodes, H. Reimerdes, D. L. Rudakov, M. J. Schaffer, G. Wang, and L. Zeng. Phys. Rev. Letters **92**, 235003 (2004).

[28] O. Neubauer, G. Czymek, K. H. Finken, B. Giesen, P. W. Hüttemann, H. T. Lambertz, J. Schruff, and TEXTOR Team. Fusion Engineering and Design **75–79** 495 (2005).

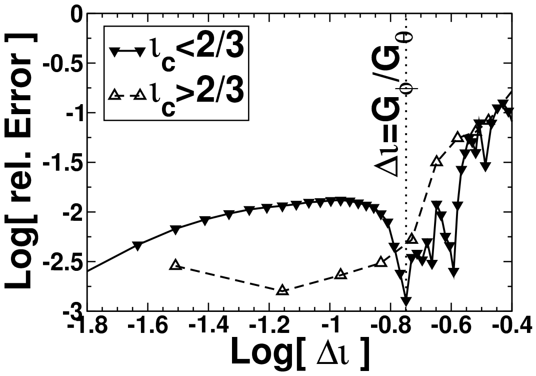

Figure 1: Numerical error in the dominant Fourier component $T_{3/2}$ of the temperature perturbation at a large $3/2$ magnetic island vs. the misalignment $\Delta\iota$. A strong increase for $\Delta\iota \gtrsim G_\phi/G_\theta$ is observed.

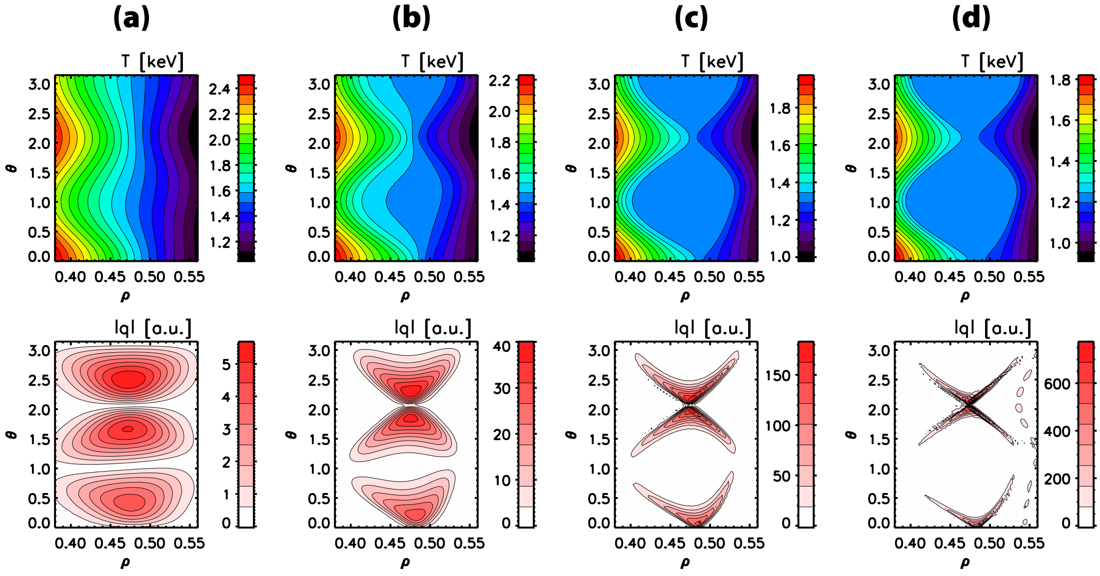

Figure 2: (Color online) Contour plots of the temperature T (top) and the heat flux density $|\vec{q}|$ (bottom) at a $3/2$ island with $w = 8.1\mathrm{cm}$. Results for $\chi = 3 \cdot 10^5$ (a), $\chi = 4 \cdot 10^6$ (b), $\chi = 7 \cdot 10^7$ (c), and $\chi = 1 \cdot 10^9$ (d) are shown, which correspond to $w/w_c = 1.1$, 2.1, 4.2, and 8.4. Low and high field side are located at $\theta = 0$ resp. $\theta = \pi$.

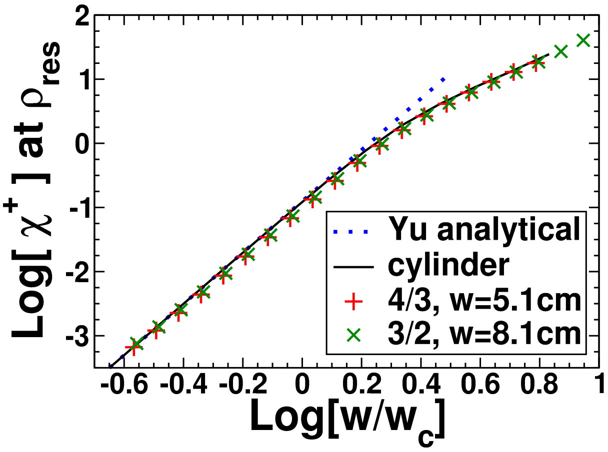

Figure 3: (Color online) Comparison of χ_ρ^+ at the resonant surface of magnetic islands. The two cases for tokamak geometry show almost perfect agreement and differ from cylindrical computations (taken from Fig. 5 of Ref. [20]) by up to 25 percent. Analytical predictions by Yu (see Appendix of Ref. [19]) which have been derived for small islands in cylindrical geometry are also plotted.

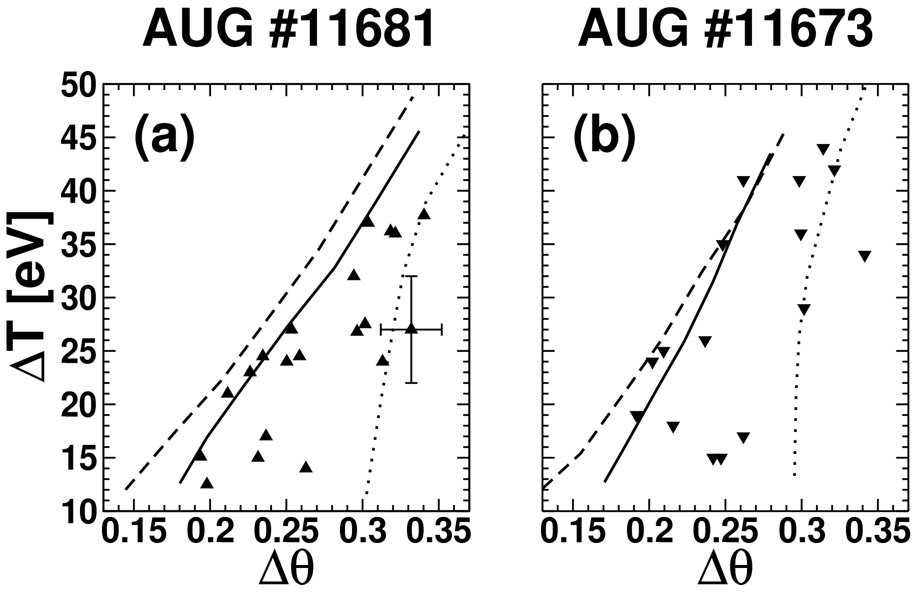

Figure 4: Height vs. width of the smallest poloidal temperature structures observed close to the island resonant surface at random timepoints of two ASDEX Upgrade discharges. The island width is about $6\mathrm{cm}$ in discharge #11681 and about $5\mathrm{cm}$ in discharge #11673. The dashed, solid and dotted curves correspond to numerical results using Spitzer-H¨arm diffusivity χ_{SH}, heat flux limit diffusivity χ_{hfl} and $\chi_{hfl}/4$. Error bars are given at one data point only for the sake of clarity.

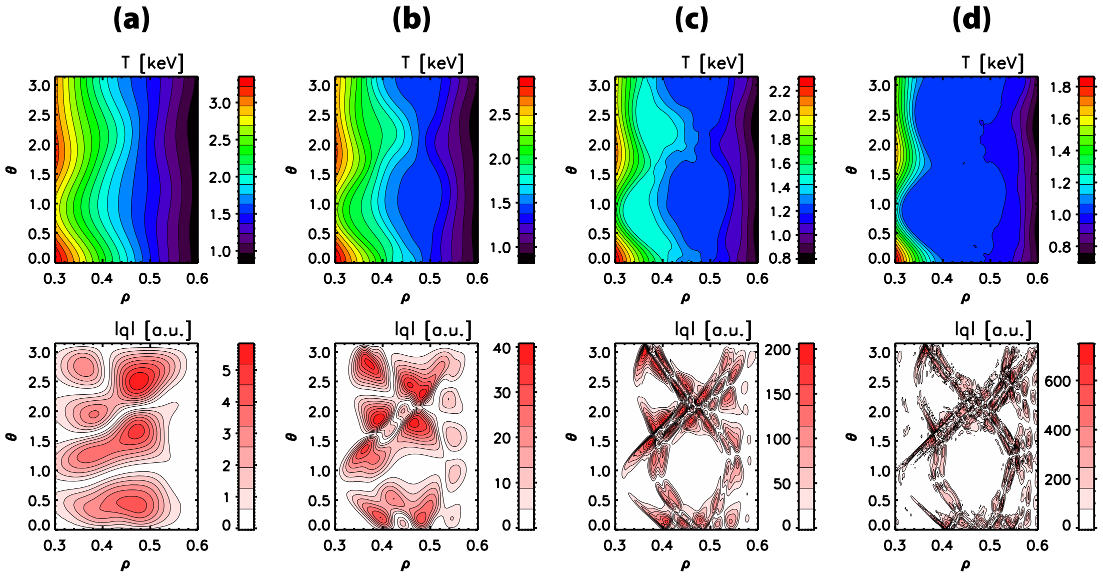

Figure 5: (Color online) Contour plots of the temperature (top) and the heat flux density $|\vec{q}|$ (bottom) at an ergodic layer produced by overlapping $3/2$ and $4/3$ islands with $w_{3/2} = 8.1\mathrm{cm}$ and $w_{4/3} = 5.1\mathrm{cm}$. Results for **(a)** $\chi = 3\cdot 10^5$, **(b)** $\chi = 4\cdot 10^6$, **(c)** $\chi = 7\cdot 10^7$, and **(d)** $\chi = 1\cdot 10^9$ are shown. Low and high field side are located at $\theta = 0$ resp. $\theta = \pi$.

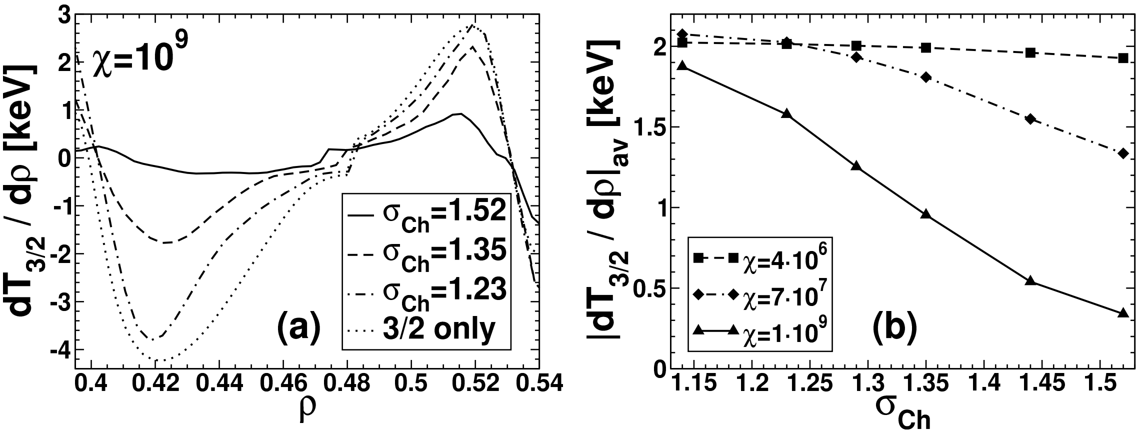

Figure 6: **(a)** Radial profile of the derivative $dT_{3/2}/d\rho$ of the first temperature harmonic. Cases with a single $3/2$ island and with an additional $4/3$ island of increasing amplitude are plotted. Results for the heat diffusion anisotropy $\chi = 10^9$ are shown. The resonant surfaces of the $3/2$ and $4/3$ islands are located at $\rho = 0.478$ resp. $\rho = 0.381$.
(b) Average of the absolute value of $dT_{3/2}/d\rho$ in the island region. The dependence on the Chirikov-Parameter σ_{Ch} is plotted for three different values of the heat diffusion anisotropy χ.

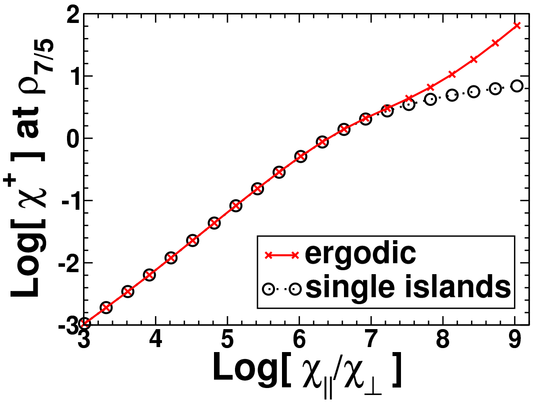

Figure 7: (Color online) Relative increase χ^+_ρ of the effective radial heat diffusivity at the $q = 7/5$ surface ($\rho_{7/5} = 0.424$) caused by overlapping $4/3$ and $3/2$ magnetic perturbations with $\sigma_{Ch} = 1.5$. Radial heat transport is strongly enhanced for large heat diffusion anisotropies χ compared to the sum of single island effects, while both are equal for small values of χ.

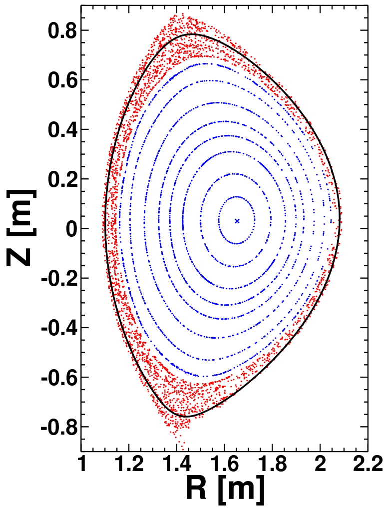

Figure 8: (Color online) Poincaré plot of the ergodic plasma boundary caused by external perturbation coils. The solid line indicates the last closed magnetic surface of the unperturbed equilibrium.

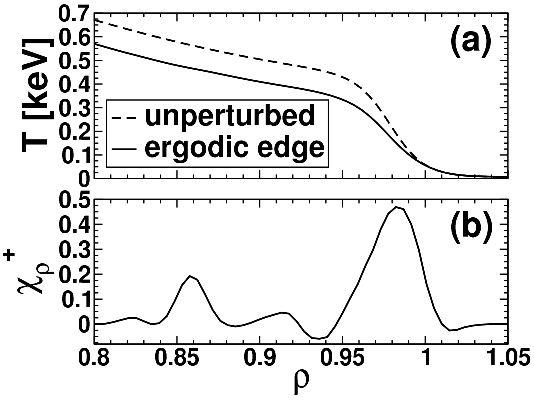

Figure 9: **(a)** Radial profile of the poloidally and toroidally averaged temperature both for the equilibrium magnetic field and for the ergodized plasma boundary.
(b) Relative increase of the radial heat diffusivity χ_ρ^+ (see Eq. 12) due to edge stochastisation.

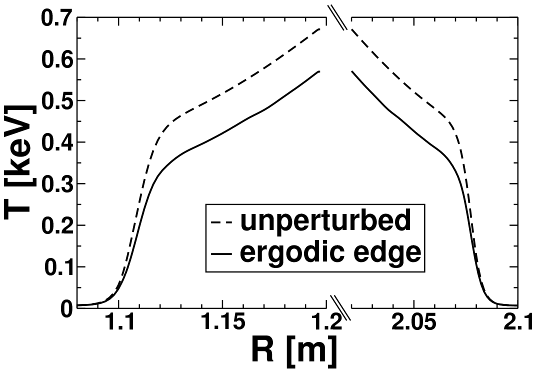

Figure 10: Temperature cuts along the major radius at the midplane of the low and high field sides for equilibrium magnetic field and the ergodized plasma boundary.